PAPER

Facile one-pot synthesis of 3D graphite–SiO₂ composite foam for negative resistance devices†

Ye Wu, [a] Hao Fu, [b] Amitava Roy,[c] Pengfei Song,[b] Yingcheng Lin,*[de] Orhan Kizilkaya*[c] and Jian Xu*[a]

In this study, we successfully prepare a porous graphite–SiO₂ composite foam *via* a facile glucose-foaming-based method. The foam was characterized by XRD, XPS, SEM, Raman, and soft X-ray absorption spectroscopy of the carbon and oxygen K-edges and by silicon K-edge X-ray absorption near edge structure (XANES) spectroscopy. The electrical properties of the sample were evaluated using current–voltage measurements. The synthesized graphite–SiO₂ composite foam showed negative resistance effect, *i.e.* an increase in the applied voltage led to a decrease in current. This negative resistance effect can be explained by two possible mechanisms: (1) the existence of defect states and (2) a change in the charge shifting amount.

Introduction

The electronic properties of carbon materials have been actively explored for decades. The electronics of graphite,[1] carbon nanotubes,[2] fullerene,[3] and graphene[4] are generally well understood. Research on the electronics of carbon structures has focused on 3D carbon composites[5–20] in recent years.

Nonlinear electrical responses, which emerge as capacitive[5–10] and electrical switch[11]/transistor-like[12] behavior, have been observed in several 3D carbon based electrical materials and devices. Thus, much attention has been given to the development of potentially novel electronic devices, as well as to understanding fundamental transport properties.

One of the motivations for research on 3D carbon composites based electrical materials and devices is that the 3D structure provides much more contact areas than the 2D structure in practical electronic applications. Another motivation is that 3D carbon electrodes are beneficial for compact integration in super large-scale integrated circuits.

One actively studied approach to fabricate 3D carbon composites is to use graphene to wrap polymers or carbon nanotubes or metal oxides nanoparticles[5–10] since the 2D structure of graphene is flexible. However, these methods are complicated due to the difficulty in synthesizing graphene. As a result, graphene oxides are typically used as the agent for introducing graphene.[5–10] However, this approach involves sophisticated chemistry, which utilizes strong acids and strong oxidizers in complex steps for the synthesis of graphene oxide.[5–10] Another possible approach is to use graphite foam as a 3D carbon network or template for introducing guest molecules.[13–20] Graphite foam could be prepared by foaming organic precursors[21–24] such as sucrose[22,23] or bread,[24] followed by carbonization.

The negative resistance effect has been investigated in Al–Al₂O₃–metal,[25] SnS₂/ZrS₂ (ref. 26), InSb,[27] organic materials,[28] AlAs/GaAs[29] based devices, a resonant tunneling diode,[30] a grid-gate modulation-doped field-effect transistor,[31] PbSnTe/PbTe double heterojunction diodes[32] and paper based devices.[33] To date, to the best of our knowledge, there has been no report on the negative resistance effect in 3D carbon composite foams.

In this study, we report that 3D graphite–SiO₂ foam can be easily synthesized by foaming glucose. The material is characterized *via* XRD, XPS, SEM, Raman, soft X-ray absorption spectroscopy of the carbon and oxygen K-edges, and silicon K-edge XANES. The resulting devices show the negative resistance effect since their channel current tends to decrease when a pole voltage is applied. This behavior is explained by two possible mechanisms: (1) the existence of defect states and (2) a change in the charge shifting amount. Due to the new fabrication method and its exceptional performance, the 3D graphite–SiO₂ foam is envisioned to play significant roles in many low-cost, rapidly processed and large-area macroelectronic applications.

[a]Division of Electrical and Computer Engineering, College of Engineering, Louisiana State University, Baton Rouge, LA 70803, USA. E-mail: jianxu1@lsu.edu

[b]Department of Mechanical Engineering, McGill University, 817 Sherbrooke St. West, Room 270, Montreal, Quebec H3A 0C3, Canada

[c]Center for Advanced Microstructures & Devices, Louisiana State University, 6980 Jefferson Highway, Baton Rouge, LA 70806, USA. E-mail: orhan@lsu.edu

[d]Key Laboratory of Dependable Service Computing in Cyber Physical Society (Chongqing University) of Ministry of Education, Chongqing 400044, China. E-mail: linyc@cqu.edu.cn

[e]College of Communication Engineering, Chongqing University, Chongqing 400044, China

† Electronic supplementary information (ESI) available. See DOI: 10.1039/c7ra07465d

Results and discussion

The graphite–SiO$_2$ foam was synthesized *via* a self-developed glucose-foaming technology, as described in Fig. 1a, which involved dehydration, heating and carbonization. Initially, a cup of black-grey gel was formed by mixing and stirring melted glucose (20 g), silicon powder (4.7 g) and boric acid (1.6 g) for 15 minutes. The gel was poured into a steel pot (inner diameter: 53 mm; outer diameter: 60 mm; and height: 42 mm). The configuration of the steel pot is shown in Fig. 1b; a cutter was inside the steel pot, which could be manually rotated. The cutter was made using a copper sheet and was used to take out the sample foam from the pot in the final step of the synthesis. A steel cover (diameter: 80 mm and height: 25 mm) was put on the top of the pot in order to prevent the gel from blowing out of the pot when heat was applied. It should be noted that the volume of the gel inside the pot played an important role in the successful synthesis. When too much of the gel was heated, it expanded and raised the steel cover. It is recommended that the volume of the gel be around 20–40% of the total volume of the pot. The gel was dehydrated after heating in a programmable furnace at 120 °C for 4 hours. A furnace rather than a hot plate is recommended since a furnace generates heat uniformly. If a hot plate is used, it is recommended that the dehydration step is carried out for a longer period.

The dehydrated gel was carbonized by heating it further at 250 °C for 5 hours. When the gel was heated, the wall and the cover of the pot forced the gel to form a cylinder and the hot air inside the pot blew the gel from time to time. Therefore, a porous foam was formed after this operation. This foam was first heated at 400 °C for 5 h and then at 1100 °C for 2 hours. It should be noted that the cooling process from 1100 °C to room temperature was set to be as fast as possible in order to prevent
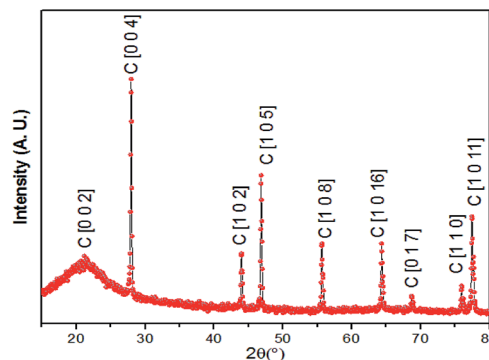

Fig. 2 XRD pattern of the graphite–SiO$_2$ composite foam.

overheating of the samples. The typical cooling duration was around 4 hours. When the foam was cooled, the pot was taken out of the furnace. The steel cover was found to be adhered to the pot, and it was removed using a hammer. By rotating the cutter of the pot, the foam was taken out of the pot.

The resulting foam was characterized *via* X-ray powder diffraction (XRD), Raman spectroscopy, scanning electronic microscopy (SEM), soft X-ray absorption spectroscopy of the carbon and oxygen K-edges and silicon K-edge X-ray absorption near edge structure (XANES) spectroscopy. The experimental XRD profile is shown in Fig. 2, in which the phases of graphite are identified and crystalline phases of SiO$_2$ are not observed. The phases of SiO$_2$ were further confirmed to be amorphous in the silicon K-edge XANES spectra (Fig. 7), which will be discussed later.

X-ray photoelectron spectroscopy (XPS) was applied to quantify the elements of the samples. The detailed quantification is listed in Table 1 and the XPS spectra are shown in Fig. 3. The XPS survey spectra are presented in the ESI.† The binding energy of C 1s of graphite, Si 2p of SiO$_2$ and O 1s of SiO$_2$ is 285.30 eV, 105.36 eV and 534.51 eV, respectively.

Table presents details of the XPS parameters. The dominant element is found to be O 1s, and the atomic concentrations of Si 2p and C 1s are approximately equal.

The Raman spectra (Fig. 4) show prominent peaks at 190 cm^{-1}, 412 cm^{-1}, 451 cm^{-1}, 583 cm^{-1}, 794 cm^{-1}, 921 cm^{-1}, 1155 cm^{-1}, 1329 cm^{-1}, 1594 cm^{-1}, 2543 cm^{-1} and 2658 cm^{-1}. The sample exhibits the prominent peak of graphite at 1329 cm^{-1} (D peak), 1594 cm^{-1} (G peak) and 2658 cm^{-1} (G′ peak).[34] The peaks at 190 cm^{-1}, 412 cm^{-1}, 451 cm^{-1} and 794 cm^{-1} are due to the vibrations of the Si–O bond.[35,36] The peak at 921 cm^{-1} is associated with the Si–OH stretching mode (here, H element could be generated from the starting material, glucose).[36] The peak at 583 cm^{-1} is attributed to the vibrations
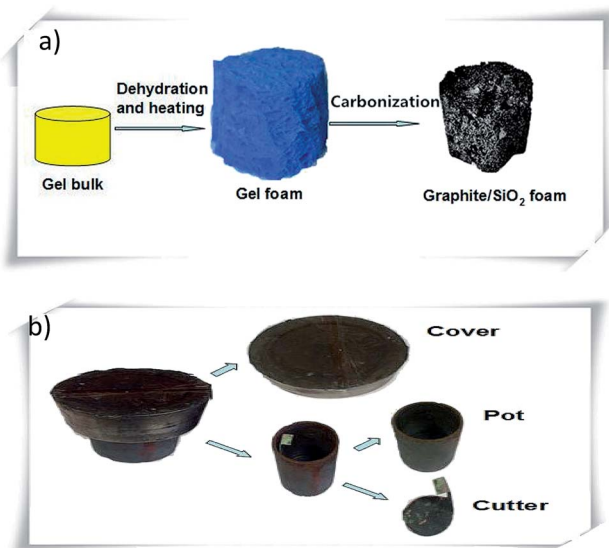

Fig. 1 (a) Schematic of the synthesis of the graphite–SiO$_2$ foam. (b) Schematic of the pot used for the synthesis of the graphite–SiO$_2$ foam.

Table 1 XPS parameters for the graphite–SiO$_2$ composite foam

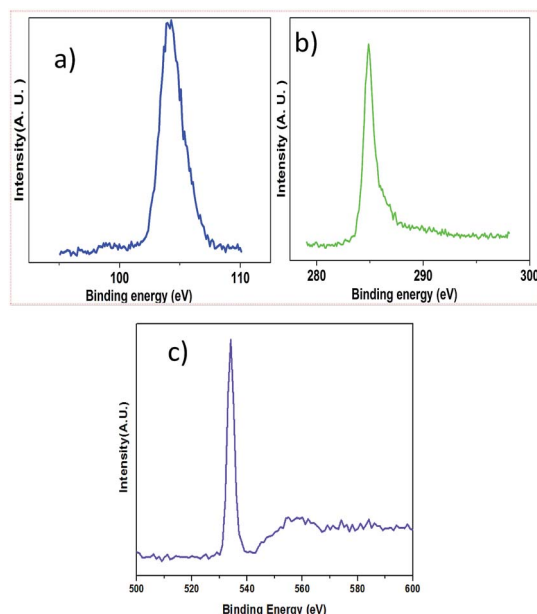| Name	Peak BE	FWHM eV	Area (P) CPS eV	Atomic%
O 1s	534.51	3.85	116 562.69	48.24
Si 2p	105.36	3.97	22 868.26	22.78
C 1s	285.30	2.77	29 019.42	28.98

Fig. 3 (a) XPS spectrum corresponding to Si 2p; (b) XPS spectrum corresponding to C 1s and (c) XPS spectrum corresponding to O 1s.

of the bridging oxygen in the Si–O–Si linkages.[36] The peaks below 1500 cm^{-1} such as those at 1155 cm^{-1} and 1329 cm^{-1} are associated with the vibrational features of sp^3 bonded carbons. The peak at around 2700 cm^{-1} (which is exactly at 2658 cm^{-1}) is generally considered as the second order of the D peak or the 2D peak.[34] The peaks at 1594 cm^{-1} and 2543 cm^{-1} are due to the defect states or the decomposition of the D peak and 2D peak of graphite. It should be mentioned that several sharp but weak Raman peaks appear at 486 cm^{-1}, 492 cm^{-1}, 496 cm^{-1},
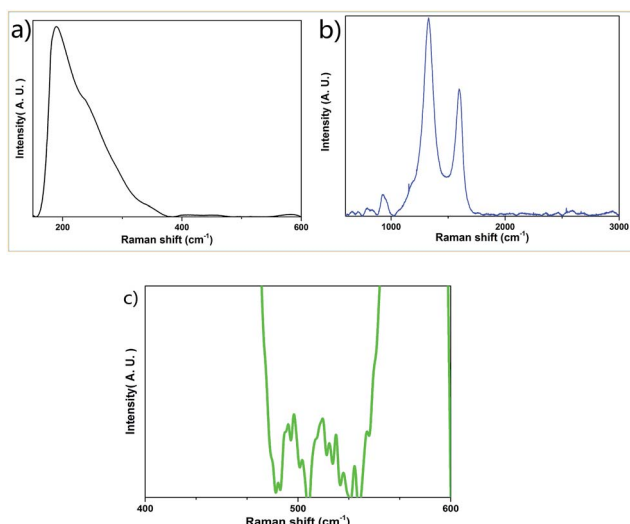

Fig. 4 (a) Raman spectrum of the graphite–SiO$_2$ composite foam in the range of 100 cm^{-1} to 600 cm^{-1}. (b) Raman spectrum of the graphite–SiO$_2$ composite foam in the range of 600 cm^{-1} to 3000 cm^{-1}. (c) Non-prominent Raman peaks of the graphite–SiO$_2$ composite foam in the range of 485 cm^{-1} to 540 cm^{-1}. (The excitation wavelength was 632.80 nm).

503 cm^{-1}, 516 cm^{-1}, 521 cm^{-1}, 524 cm^{-1}, 530 cm^{-1} and 538 cm^{-1} (Fig. 4c). These peaks are due to the vibrations of O–B–O bending,[37] which originates from the thermal decomposition of boric acid, one of the starting materials in the synthetic process.

The surface morphology of the foam was characterized *via* SEM. During the imaging process, a 5 kV beam accelerating voltage was applied. The SEM image (Fig. 5a) shows the porous structure of the foam sample surface. The enlarged SEM image (Fig. 5b) clearly shows that the sample surface is rough.

Complementary to the X-ray photoelectron measurements of the occupied core electron states, XANES measurements allow the unoccupied states (partial density of electron states) of a sample to be probed. The carbon K-edge XANES spectra of the graphite–SiO$_2$ foam and graphite foil were obtained and depicted in Fig. 6a. The two prominent peaks centered at 285.40 eV and 292.00 eV in the graphite foil absorption spectrum are resonances from the 1s → π* and 1s → σ* (sp^2) electron transitions, respectively.[38,39] With reference to the absorption spectrum of the graphite foil in Fig. 6a, it is clear that the graphite–SiO$_2$ foam sample has the same transitions as the graphite foil. The strong peak from the 1s → π* transition indicates the graphitic structure of the graphite–SiO$_2$ foam.

It should be noted that the intensity of the shoulder and peak centered at around 288 eV between the π* and σ* transitions in Fig. 6a is enhanced. These features were reported in the previous work[38,39] on graphite-related samples and were assigned to the 1s → π* transition from the C–O bond (286.00 eV) and the 1s → σ* transition (288.70 eV) from the aliphatic carbon and/or defect states. The X-ray photoelectron spectrum of the graphite–SiO$_2$ foam (Fig. 3c) confirms C–O bond formation in the graphite–SiO$_2$ foam as a shoulder located at 286 eV, which is attributed to the C–O functional group. Besides the carbon K-edge, we collected the oxygen K-edge absorption spectra of the graphite–SiO$_2$ foam to gain further insight into its electronic structure.

The oxygen K-edge XANES spectra of the graphite–SiO$_2$ foam and quartz reference sample are displayed in Fig. 6b. The red line of the quartz oxygen K-edge XANES spectrum centered at 537.60 eV originates from the transition of the 1s electron to 2p electron states hybridized with the silicon 3s and 3p states in the tetrahedrally coordinated SiO$_2$. The pre-edge peak that is apparent from the main edge at 532.00 eV was observed in
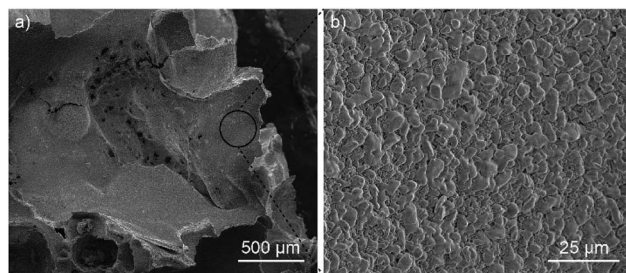

Fig. 5 (a) SEM image of the graphite–SiO$_2$ foam surface. (b) Enlarged SEM image of the region marked with a black circle in (a). The scale bars in (a) and (b) are 500 μm and 25 μm, respectively.
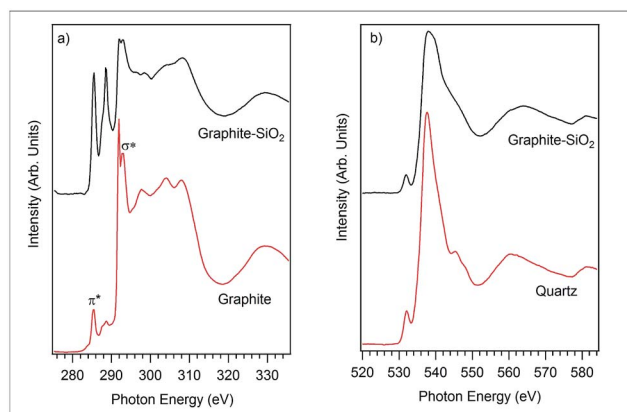
Fig. 6 (a) Carbon K-edge XANES spectra of graphite and the graphite–SiO$_2$ foam and (b) oxygen K-edge XANES spectra of quartz and the graphite–SiO$_2$ foam.

previous SiO$_2$ studies and is considered to originate from the O 1s electron transition to the π^* orbital states of O$_2$.[40]

Comparing the structure and features of the oxygen K-edge spectrum of the graphite–SiO$_2$ foam with that of quartz, we observed no significant differences between the two spectra. However, we noticed that the oxygen K-edge of the graphite–SiO$_2$ foam shows smoother features in the post edge XANES region (above 540 eV) compared to the XANES spectrum of quartz. These findings indicate that the graphite–SiO$_2$ foam possess some imperfections in its silicon dioxide layer. The silicon K-edge XANES spectra of the graphite–SiO$_2$ foam (Fig. 7) also confirm the imperfection in the silicon dioxide layers of the composite.

Fig. 7 shows the Si K-edge XANES spectra of the graphite–SiO$_2$ composite along with that of crystalline and amorphous SiO$_2$ and a silicon powder. The comparison shows that the SiO$_2$
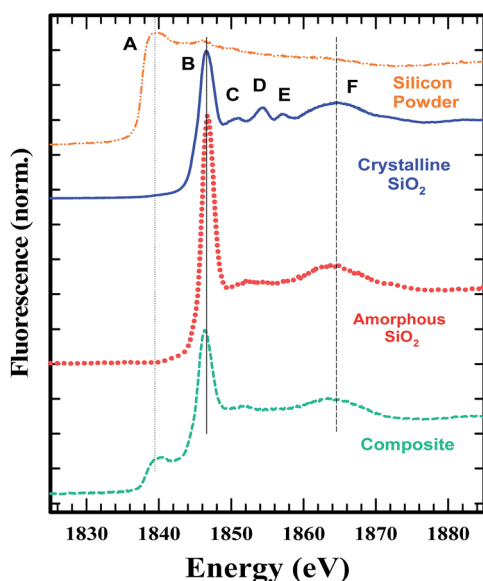
in the composite is amorphous. The smaller D and E peaks seen in the crystalline SiO$_2$ are absent in the composite, similar to the amorphous SiO$_2$. The C peak, which is less pronounced, is present in the composite, similar to the amorphous silica. A comparison of the composite spectra with that of the silicon powder shows that some of the starting material remained in the sample.

Fig. 8 is the electrical measurement configuration. Silver gel was used in order to make close contact between the electrical wires and the sample.

As shown in Fig. 9, the current I_2 increases with an increase in the voltage V_2 (Fig. 9a), which satisfies Ohm's law. However, I_2 decreases with an increase in the voltage V_1 (Fig. 9b), which is indeed a negative resistance effect and contrary to Ohm's law.

There is no decisive conclusion about the origin of the negative resistance effect, which is considered to be due to the potential barrier enhancement,[25] excitation of the domain-wall,[26] resonant tunneling,[30] impurity band conduction,[29] and construction of localized electrical polarization.[33]

In order to explain this effect, two possible mechanisms are proposed as follows.

The first possible mechanism is due to the existence of defect states in the composite foam. As derived from Table 1, the atomic ratio of oxygen-to-silicon is 2.12, which indicates that O 1s is redundant. These redundant O 1s could combine with the small amount of the remaining starting materials (such as C and H from glucose and B from boron acid) to form a complex structure which is undetectable in the Raman/XANES spectra due to the resolution limitation of the instruments or appears as small peaks in the spectra profile. This is consistent with the findings from the Raman/XANES spectra. As mentioned in the paragraph describing the Raman spectra, the Raman peaks at 486 cm^{-1}, 492 cm^{-1}, 496 cm^{-1}, 503 cm^{-1}, 516 cm^{-1}, 521 cm^{-1}, 524 cm^{-1}, 530 cm^{-1} and 538 cm^{-1} are attributed to the vibration of O–B–O bending and the peak at 921 cm^{-1} is considered due to the Si–OH stretching mode. Also, as stated in the XANES section, two peaks from XANES indicate the formation of C–O bond (286.00 eV)/defect states (288.70 eV). They are certain sources of defects existing in the composite foam. The dielectric constant for the electrons around these defects would be higher.[41] The Bohr radius can be calculated as[41]
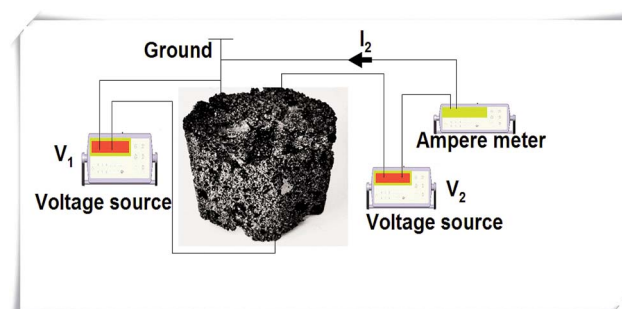

Fig. 7 Silicon K-edge XANES of the graphite–SiO$_2$ foam.

Fig. 8 Electrical measurement diagram for the sample, where V_1 and V_2 are the applied voltage and I_2 represents the current.

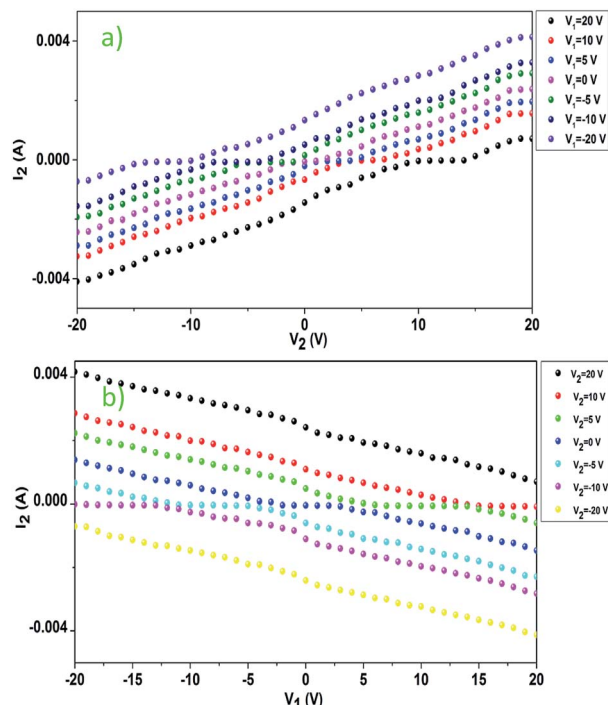**Fig. 9** Current dependence on voltage: (a) I_2 vs. V_2 when V_1 is different and (b) I_2 vs. V_1 when V_2 is different.

Fig. 10 (a) Process for the formation of electrical coupling due to the existence of defect states. The electrons around the defect states first occupy the region with a higher Bohr radius and form an extra band. Then, the interactions between these electrons and the empty states of other atoms produce electrical polarization and electric coupling is introduced. (b) Simulated result of the current vs. charge shifting amount.

$$\alpha_{\mathrm{H}} = \frac{\hbar^2 \kappa}{me^2} \qquad (1)$$

where, κ is the permittivity, m is the electron mass and e is the electron charge. The electrons with a higher dielectric constant would occupy large Bohr orbitals. These electrons would also form an extra band. The potential energy of the electron at a certain distance r is defined as[41]

$$V = \frac{e^2}{r\kappa(\omega, T)} \qquad (2)$$

where, $\kappa(\omega, T)$ is the high-frequency permittivity. Based on the dielectric theory, the permittivity $\kappa(\omega, T)$ is written as:[42]

$$\kappa(\omega, T) = \frac{B(\omega, T)}{1 + C(\omega, T)} \qquad (3)$$

where, $B(\omega, T)$ and $C(\omega, T)$ are functions of temperature T and frequency ω, respectively.

Given that the permittivity is dependent on temperature, the potential is associated with the temperature. When an external voltage is applied on the sample, it causes the temperature to increase. Therefore, the potential is subjected to external modulation of the electrical voltage. In this way, the variation in the potential is introduced by voltage modulation. Interactions between the extra band and empty states of the atoms appear and some the electrons from the defects could transit between the extra band and the side of the atoms. Therefore, electric polarization appears in the extra band and electrical coupling is introduced (Fig. 10a).
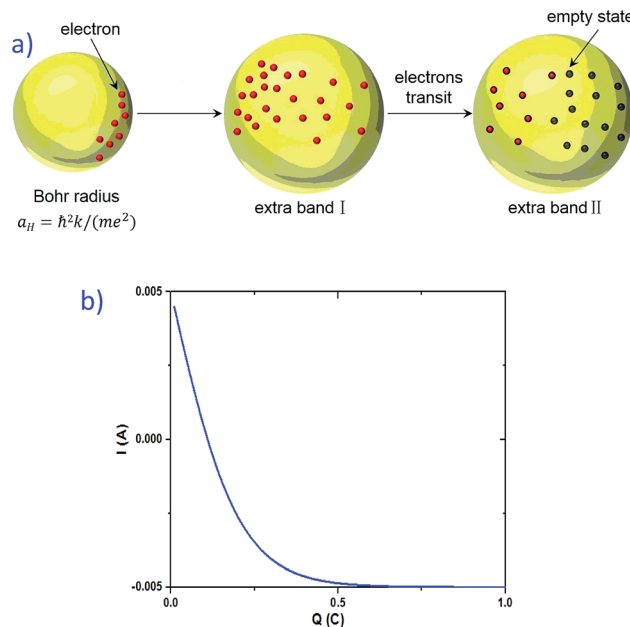
If the direction of the electric polarization contributed from the extra band is in contrast to that of the electric field applied, it will harm the output current and even change its direction. When a higher electrical field is applied, the variation in potential becomes larger. At the same time, opposite electric polarization is introduced. Therefore, the output current becomes smaller. In this way, the negative resistance effect becomes active.

Another possible mechanism is the change in the charge shift amount (see the ESI for a detailed theoretical derivation†). When a voltage is applied to the sample, the charge shifts due to the existence of a localized electric field. The current derived is dependent on the amount of the charge that is shifted by the electrical field (see eqn (S.24) in the ESI†). Fig. 10b presents the simulated result of I vs. Q. The increase in the charge shifting amount leads to a decrease in the current, which is a possible explanation for the negative resistance effect in the graphite–SiO_2 foam.

Experimental

Materials

The raw materials used to synthesize the graphite–SiO_2 foam include melted-glucose (CK Products, LLC., USA), silicon powder (Johnson Matthey Catalog Company, USA) and boric acid (Fisher Scientific Company, Chemical Manufacturing Division, USA).

SEM, XRD, XPS and Raman characterization

The prepared foams were studied *via* electron microscopy, Raman spectroscopy and X-ray diffraction. SEM was conducted using an FEI Quanta 200 SEM. Raman spectroscopy was performed using a Johin Yvon Horiba LABRAM Integrated Raman Spectroscopy System using an HeNe laser (wavelength: 632.81 nm). XRD patterns were collected using a Shimazu XRD-6000 with Cu Kα radiation of 1.5406 Å. XPS analyses were conducted using a K-α XPS instrument (Thermo Scientific, USA).

Soft X-ray absorption spectroscopy of the carbon and oxygen K-edge

Soft X-ray absorption spectroscopy of the carbon and oxygen K-edges was performed at the variable-line-space plane-grating-monochromator (VLSPGM) beamline of the Center for Advanced Microstructures and Devices (CAMD), Louisiana State University, Baton Rouge, Louisiana, USA. The beamline that provides a resolution better than 0.20 eV at the carbon K-edge has been described in detail elsewhere.[43] The soft X-ray beamline monochromator delivered monochromatic photons in the energy range of 180–1000 eV with two interchangeable gratings. We collected the absorption spectra using the total electron yield technique by measuring the sample's drain current with a 0.20 eV energy step size. The spectra were normalized to the primary beam current acquired from the gold sputtered mesh. The base pressure of the chamber was at 2×10^{-9} Torr. We exploited a graphite foil and powdered quartz reference samples to calibrate the energy scale of the grating and identify the absorption features on the graphite–SiO_2 foam sample.

Silicon K-edge XANES spectra measurement

Silicon K-edge XANES spectra of the composite and relevant silicon standards were measured at the Low Energy X-ray Absorption Spectroscopy (LEXAS) Beamline of J. Bennett Johnston, Sr. in CAMD. CAMD operates an electron storage ring at 1.30 GeV. LEXAS is a windowless beamline with only a 13 μm thin Kapton window separating the ring from the experimental station. Measurements were made using a University of Bonn modified LeMonnier-type double crystal monochromator. InSb 111 crystals were used at this energy. The scan boundaries were 1800 eV to 1830 eV with 0.50 eV steps, 1830 eV to 1870 eV with 0.10 eV steps, and 1870 eV to 1910 eV with 0.30 eV steps. The measurements conducted *via* fluorescence with an 80 mm² Ketek™ silicon drift detector. The material was diluted with boron nitride to keep the detector dead time low. The high dead time reduced the white line intensity. The integration time was varied from 3 to 5 seconds to obtain appropriate counting statistics. At least two spectra were collected. Data were analyzed using a Demeter and Athena system.[44]

Conclusions

A graphite–SiO_2 composite foam was synthesized using glucose as a foaming agent. The fabricated graphite–SiO_2 composite foam shows the negative resistance effect. This effect is considered to occur due to two possible mechanisms: (1) the existence of defect states and (2) change in the charge shifting amount. Due to the use of simple chemistry and the negative resistance effect, our technique may provide a rapid processing method to fabricate electric devices for a variety of macro-electronic applications.

Conflicts of interest

There are no conflicts to declare.

Acknowledgements

References

1 B. Sun and M. Skyllas-Kazacos, *Electrochim. Acta*, 1992, **37**, 2549.

2 T. W. Ebbesen, H. J. Lezec, H. Hiura, J. W. Bennett, H. F. Ghaemi and T. Thio, *Nature*, 1996, **382**, 54.

3 R. A. Jishi, M. S. Dresselhaus and G. Dresselhaus, *Phys. Rev. B*, 1993, **48**, 11385.

4 E. H. Hwang, S. Adam and S. Das Sarma, *Phys. Rev. Lett.*, 2007, **98**, 186806.

5 X.-C. Dong, H. Xu, X.-W. Wang, Y.-X. Huang, M. B. Chan-Park, H. Zhang, L.-H. Wang, W. Huang and P. Chen, *ACS Nano*, 2012, **6**, 3206–3213.

6 X. Cao, Y. Shi, W. Shi, G. Lu, X. Huang, Q. Yan, Q. Zhang and H. Zhang, *Small*, 2011, **7**, 3163–3168.

7 W. Chen, S. Li, C. Chen and L. Yan, *Adv. Mater.*, 2011, **23**, 5679–5683.

8 L. Zhang, F. Zhang, X. Yang, G. Long, Y. Wu, T. Zhang, K. Leng, Y. Huang, Y. Ma, A. Yu and Y. Chen, *Sci. Rep.*, 2013, **3**, 1408.

9 W. Wei, S. Yang, H. Zhou, I. Lieberwirth, X. Feng and K. Müllen, *Adv. Mater.*, 2013, **25**, 2909–2914.

10 D.-W. Wang, F. Li, M. Liu, G. Q. Lu and H.-M. Cheng, *Angew. Chem., Int. Ed.*, 2008, **47**, 373–376.

11 P. S. Dorozhkin, S. V. Tovstonog, D. Golberg, J. Zhan, Y. Ishikawa, M. Shiozawa, H. Nakanishi, K. Nakata and Y. Bando, *Small*, 2005, **1**, 1088–1093.

12 J.-M. Ting, T.-P. Li and C.-C. Chang, *Carbon*, 2004, **42**, 2997–3002.

13 J. Ji, L. L. Zhang, H. Ji, Y. Li, X. Zhao, X. Bai, X. Fan, F. Zhang and R. S. Ruoff, *ACS Nano*, 2013, **7**, 6237–6243.

14 J. Ji, H. Ji, L. L. Zhang, X. Zhao, X. Bai, X. Fan, F. Zhang and R. S. Ruoff, *Adv. Mater.*, 2013, **25**, 4673–4677.

15 X. Xia, D. Chao, Z. Fan, C. Guan, X. Cao, H. Zhang and H. J. Fan, *Nano Lett.*, 2014, **14**, 1651–1658.

16 D. Chao, X. Xia, J. Liu, Z. Fan, C. F. Ng, J. Lin, H. Zhang, Z. X. Shen and H. J. Fan, *Adv. Mater.*, 2014, **26**, 5794–5800.

17 J. Ji, J. Liu, L. Lai, X. Zhao, Y. Zhen, J. Lin, Y. Zhu, H. Ji, L. L. Zhang and R. S. Ruoff, *ACS Nano*, 2015, **9**, 8609–8616.

18 Y. Chen, Z. Zhang, Z. Sui, Z. Liu, J. Zhou and X. Zhou, *Int. J. Hydrogen Energy*, 2016, **41**, 12136–12145.

19 J. Tolvanen, J. Hannu, M. Nelo, J. Juuti and H. Jantunen, *Smart Mater. Struct.*, 2016, **25**, 1–12.

20 Y. Tong, X. Yu and G. Shi, *Phys. Chem. Chem. Phys.*, 2017, **19**, 4821–4826.

21 M. Inagaki, J. Qiu and Q. Guo, *Carbon*, 2015, **87**, 128–152.

22 K. Prabhakaran, P. K. Singh, N. M. Gokhale and S. C. Sharma, *J. Mater. Sci.*, 2007, **42**, 3894–3900.

23 C. Wang, M. J. O'Connell and C. K. Chan, *ACS Appl. Mater. Interfaces*, 2015, **7**, 8952–8960.

24 Y. Yuan, Y. Ding, C. Wang, F. Xu, Z. Lin, Y. Qin, Y. Li, M. Yang, X. He, Q. Peng and Y. Li, *ACS Appl. Mater. Interfaces*, 2016, **8**, 16852–16861.

25 T. W. Hickmott, *J. Appl. Phys.*, 1962, **33**, 2669.

26 P. A. Lee, *Solid State Commun.*, 1969, **7**, 1359–1361.

27 S. Itoh, Y. Ohta and H. Fujiyasu, *Appl. Phys. Lett.*, 1977, **31**, 701–703.

28 Y. Iwasa, T. Koda, S. Koshihara, Y. Tokura, N. Iwasawa and G. Saito, *Phys. Rev. B*, 1989, **39**, 10441.

29 H. S. Majumdar, J. K. Baral, R. Osterbacka, O. Ikkala and H. Stubb, *Org. Electron.*, 2005, **6**, 188–192.

30 M. Tsuchiya, H. Sakaki and J. Yoshino, *Jpn. J. Appl. Phys.*, 1985, **24**, L466–L468.

31 K. Ismail, W. Chu, A. Yen, D. A. Antoniadis and H. I. Smith, *Appl. Phys. Lett.*, 1989, **54**, 589–591.

32 A. Yasuda, K. Suto and J.-i. Nishizawa, *Results Phys.*, 2016, **6**, 41–42.

33 Y. Wu, H. Fu, B. Li and Y. Lin, *Mater. Express*, 2017, **7**, 5–14.

34 S. Reich and C. Thomsen, *Philos. Trans. R. Soc., A*, 2004, **362**, 2271–2288.

35 F. L. Galeener, J. C. Mikkelsen Jr, R. H. Geils and W. J. Mosby, *Appl. Phys. Lett.*, 1978, **32**, 34–36.

36 P. F. McMillan and R. L. Remmele Jr, *Am. Mineral.*, 1986, **71**, 772–778.

37 R. R. Servoss and H. M. Clark, *J. Chem. Phys.*, 1957, **26**, 1175–1178.

38 Y. V. Fedoseeva, G. A. Pozdnyakov, A. V. Okotrub, M. A. Kanygin, Y. V. Nastaushev, O. Y. Vilkov and L. G. Bulusheva, *Appl. Surf. Sci.*, 2016, **385**, 464–471.

39 M. Abbas, Z. Y. Wu, J. Zhong, K. Ibrahim, A. Fiori, S. Orlanducci, V. Sessa, M. L. Terranova and I. Davoli, *Appl. Phys. Lett.*, 2005, **87**, 051923.

40 G. S. Henderson, D. R. Neuville and L. Cormier, *Chem. Geol.*, 2009, **259**, 54–62.

41 N. F. Mott, *Conduction in Noncrystalline Materials*, Clarendon, Oxford, 1987.

42 Z.-Y. Cheng, R. S. Katiyar, X. Yao and A. S. Bhalla, *Phys. Rev. B*, 1998, **57**, 8166–8177.

43 M. Ono, J. D. Scott and E. Morikawa, *AIP Conf. Proc.*, 2004, **705**, 364.

44 B. Ravel and M. Newville, *J. Synchrotron Radiat.*, 2005, **12**, 537–541.